AutoGDeterm: Automatic Geometry Determination for Electron Tomography

Yu Chen, Zihao Wang, Lun Li, Jingrong Zhang, Xiaohua Wan, Fei Sun*, and Fa Zhang*

Abstract: Electron Tomography (ET) is an important method for studying cell ultrastructure in three-dimensional (3D) space. By combining cryo-electron tomography of frozen-hydrated samples (cryo-ET) and a sub-tomogram averaging approach, ET has recently reached sub-nanometer resolution, thereby realizing the capability for gaining direct insights into function and mechanism. To obtain a high-resolution 3D ET reconstruction, alignment and geometry determination of the ET tilt series are necessary. However, typical methods for determining geometry require human intervention, which is not only subjective and easily introduces errors, but is also labor intensive for high-throughput tomographic reconstructions. To overcome these problems, we have developed an automatic geometry-determination method, called AutoGDeterm. By taking advantage of the high-contrast re-projections of the Iterative Compressed-sensing Optimized Non-Uniform Fast Fourier Transform (NUFFT) reconstruction (ICON) and a series of numerical analysis methods, AutoGDeterm achieves high-precision fully automated geometry determination. Experimental results on simulated and resin-embedded datasets show that the accuracy of AutoGDeterm is high and comparable to that of the typical "manual positioning" method. We have made AutoGDeterm available as software, which can be freely downloaded from our website http://ear.ict.ac.cn.

Key words: electron tomography; geometry determination; human intervention; full automation; AutoGDeterm; comparable accuracy

1 Introduction

Electron Tomography (ET) is an important method for

- Yu Chen, Zihao Wang, Lun Li, Jingrong Zhang, Xiaohua Wan, and Fa Zhang are with the High Performance Computer Research Center, ICT, CAS, Beijing 100101, China. E-mail: {chenyu, wangzihao}@ict.ac.cn; lilun13@mails.ucas.ac.cn; {zhangjingrong, wanxiaohua, zhangfa}@ict.ac.cn.
- Yu Chen, Zihao Wang, Lun Li, and Jingrong Zhang are also with the University of Chinese Academy of Sciences, Beijing 100101, China.
- Fei Sun is with the Center for Biological Imaging, IBP, CAS and the National Key Laboratory of Biomacromolecules, CAS Center for Excellence in Biomacromolecules, Beijing 100101, China. E-mail: feisun@ibp.ac.cn.
- * To whom correspondence should be addressed.
  Manuscript received: 2017-09-06; accepted: 2017-11-01

studying cell ultrastructure in three-dimensional (3D) space. By combining cryo-electron tomography of frozen-hydrated samples (cryo-ET) with a sub-tomogram averaging approach[1, 2], ET has recently reached sub-nanometer resolution[3, 4]. Visualizing the high-resolution structure of macromolecular assemblies in three dimensions can provide direct insights into function and mechanism[2]. In ET, a series of two-dimensional (2D) projection micrographs (tilt series) are taken at different orientations and then used to reconstruct the 3D density of the cell ultrastructure, based on the projection-slice theorem[5]. A typical projection geometry is the single-axis tilt series in which the specimen is rotated about a single fixed axis (Y-axis) perpendicular to the optical axis (Z-axis) in the microscope[6]. The tilt angle of ET is limited to within $-70°$ to $+70°$ to ensure that a reasonable number of electrons can pass through to form reliable

images. The absence of high-tilt angles results in missing-wedge artifacts[7]. Usually, the projection environment is unstable due to mechanical instability and the inevitable transformation and deformations of the sample, which lead to a mismatch in the tilt series. To obtain a high-resolution 3D reconstruction, the projection parameters of the tilt series must first be accurately calibrated.

In recent years, the topic of alignment in ET has been widely discussed and many high-precision alignment algorithms have been proposed. These algorithms can be classified into two main types that generate either the following: (a) marker-based or (b) marker-free alignment. Marker-based alignment[8–12] requires that fiducial markers be embedded in the sample. With high-contrast conditions, fiducial markers can be precisely located, which greatly improves alignment accuracy. However, the embedding of fiducial markers may interfere with the sample and cause undesirable artifacts in the reconstruction. In contrast, marker-free alignment requires no embedding of fiducial markers in the sample. Examples include cross-correlation[13], common lines[14], iterative alignment methods that combine cross-correlation with reconstruction and re-projection[6, 15], and feature-based alignment methods that use features as fiducial markers[16–18]. Marker-free alignments are usually limited by their low Signal-to-Noise Ratio (SNR) and the intrinsic biological structure of the sample. More general treatments of the alignment problem can be found in Ref. [19].

One problem related to alignment is the determination of the reconstruction geometry, in which the geometry of the 3D reconstruction is described with respect to a fixed coordinate system, including the direction of the tilt axis (azimuth angle), the tilt angle offset, the thickness of the sample, and the z-shift of the reconstruction[9]. Some alignment algorithms (e.g., Refs. [6, 12, 17]) include the determination of geometry in the alignment procedure. However, the most common methods for determining the geometry depend on human intervention, herein referred to as "manual positioning", such as the successful and widely used ET tool IMOD[9]. In manual positioning, a boundary model is created that contains several manually selected position features of the 3D reconstruction, which is then used to calculate the geometric parameters. Although manual positioning has high accuracy, two key issues remain to be solved. First, as high-resolution sub-tomogram averaging demands high-throughput tomographic reconstructions[2], the need for human intervention in manual positioning will become a

bottleneck in any high-efficiency automatic ET alignment and reconstruction. Second, the manual selection of position features is fairly subjective and easily introduces errors, especially in cryo-ET reconstruction, in which the extremely low SNR and ray artifacts caused by the missing wedge make the position features difficult to identify.

To overcome these problems, we have developed an automatic ET geometry-determination method called AutoGDeterm. AutoGDeterm uses numerical analysis methods and re-projections of the Iterative Compressed-sensing Optimized Non-Uniform Fast Fourier Transform (NUFFT) reconstruction, a compressed-sensing-based[20, 21] ET reconstruction algorithm referred to as ICON[22]. AutoGDeterm has two advantages. First, its ICON-based reconstruction suffers less from ray artifacts and has a higher SNR[22]. Using the re-projections of ICON, AutoGDeterm realizes much clearer position features, which is essential for high-precision automatic geometry determination. Second, ICON can partially restore the unsampled information in ET reconstruction[22], and thereby generate a clear re-projection of the reconstructed volume at 90° (which is normally too blurred when identified by other ET reconstruction algorithms, such as ART[23], SIRT[24], and WBP[25]), so the azimuth angle can be directly determined. AutoGDeterm has also been developed into a software program and can be freely downloaded from our website http://ear.ict.ac.cn.

2　Method

2.1　Geometry

The geometry of ET reconstruction is shown in Fig. 1. The projection coordinate system (X, Y, Z) is fixed with respect to the microscope, with the Y-axis being the tilt axis and the Z-axis the optical axis (projection along
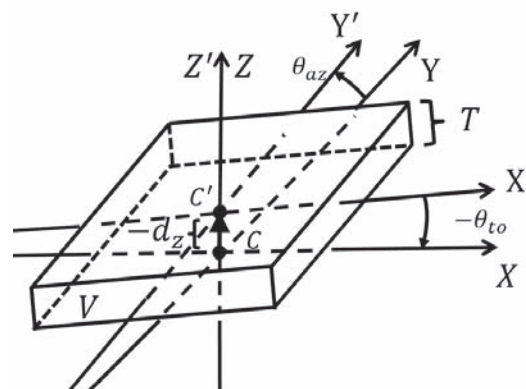

Fig. 1　The geometry of ET reconstruction.

the negative direction of the Z-axis). Volume V is the 3D density of the specimen with thickness T, which is reconstructed from the aligned tilt series. The alignment procedure aligns the tilt axis of the tilt series perpendicular to the X-axis[12]. Thus, the reconstruction coordinate system (X', Y', Z') can be defined relative to (X, Y, Z) by a rotation about the X-axis at angle θ_{az} (azimuth angle) (where the Y'-axis is the actual tilt axis), a rotation about the Y'-axis at angle $-\theta_{to}$ (where θ_{to} is the tilt angle offset) and a shift $-d_z$ along the Z-axis (where d_z is the z-shift).

Normally, alignment and geometry determination problems are intrinsically three dimensional, so errors are introduced by determining θ_{to} and θ_{az} separately using re-projections[19]. However, θ_{az} and θ_{to} are usually small for an aligned tilt series and the errors introduced by determining θ_{to} without considering θ_{az} are small enough to ignore (see Eq. (1)). So, we regard $-\theta_{to}$ as an approximate rotation about the Y-axis.

$$E_{\theta_{to}} = \theta_{to} - \theta'_{to},$$
$$\theta'_{to} = \arctan(\cos(\theta_{az}) \cdot \tan(\theta_{to})) \qquad (1)$$

where θ'_{to} is the determined tilt angle offset using re-projections in AutoGDeterm, we should notice that, before rotating by $-\theta_{to}$, the re-projection on XZ-plane is always parallel to the X-axis with any θ_{az}; $E_{\theta_{to}}$ is the error of determining θ_{to} without considering θ_{az}. When $\theta_{to} = 5°$ and $\theta_{az} = 5°$, $E_{\theta_{to}} = 0.0189°$.

2.2 ICON re-projection

ICON is an iterative ET reconstruction algorithm based on the theoretical framework of "compressed sensing". Taking advantage of prior knowledge of biological structural density and NUFFT, ICON can partially restore unsampled information, especially for the low-frequency information in Fourier space, and generate a high-contrast reconstruction[22]. Due to the limitation of tilt angles, a $-90°$ projection of specimens can not be sampled, so traditional ET reconstruction algorithms can not generate a clear $-90°$ re-projection. However, by restoring "missing information", ICON generates a much clearer $-90°$ re-projection (Fig. 2b) than WBP (Fig. 2a). With a clear $-90°$ re-projection, we can automatically determine the azimuth angle θ_{az}. To then determine the tilt angle offset, we re-project the reconstruction along the Y-axis to generate an X_{90}-re-projection. The X_{90}-re-projection of ICON (Fig. 2d) has better contrast than WBP (Fig. 2c). With this clear X_{90}-re-projection, we can automatically determine the tilt angle offset θ_{to}. We can also determine the z-shift
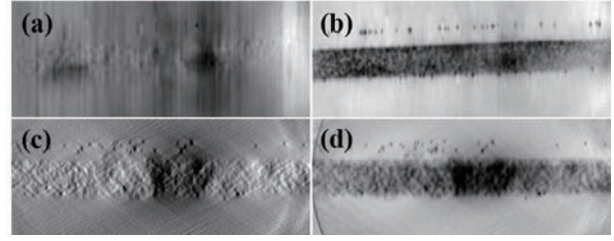

Fig. 2 $-90°$ **re-projections and** X_{90}**-re-projections of WBP and ICON (resin-embedded ET dataset is reconstructed).** (a and b) $-90°$ re-projections of WBP and ICON, respectively; (c and d) the X_{90}-re-projections of WBP and ICON, respectively.

and the thickness of the reconstructed volume using X_{90}-re-projection. Because of the ray artifacts, the thickness of the reconstructed volume is always greater than the actual thickness of the specimen. All the $-90°$ re-projections in this paper are rotated in-plane by $-90°$ and only the central areas are used for the determination.

2.3 Geometry determination

There are four geometric parameters to be determined, including the z-shift, thickness, tilt-angle offset, and azimuth angle. Figure 3 shows the AutoGDeterm workflow.

In the "**Determine z-shift & thickness**" step, we first divide the X_{90}-re-projection into a series of sub-images using a sliding window with size S_w and overlap S_o (Fig. 4a). In this paper, $S_w = 50$ and $S_o = 40$. Then, for each sub-image, we re-project it along the X-axis and normalize this re-projection to generate a normalized (in the range [0, 1]) 1D re-projection (solid line in Fig. 4b). This normalized 1D re-projection approximates a rectangular function (dashed line in Fig. 4b, generated
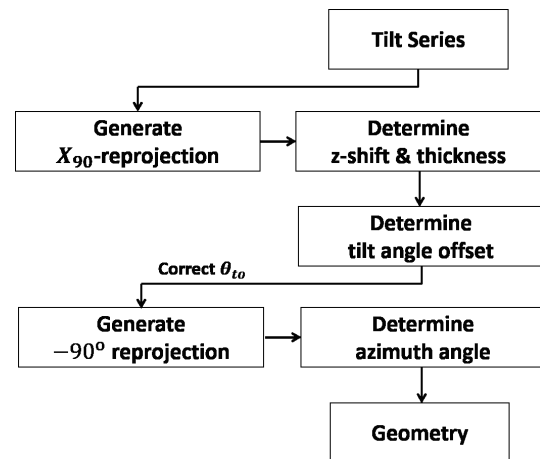

Fig. 3 The geometry of ET reconstruction.
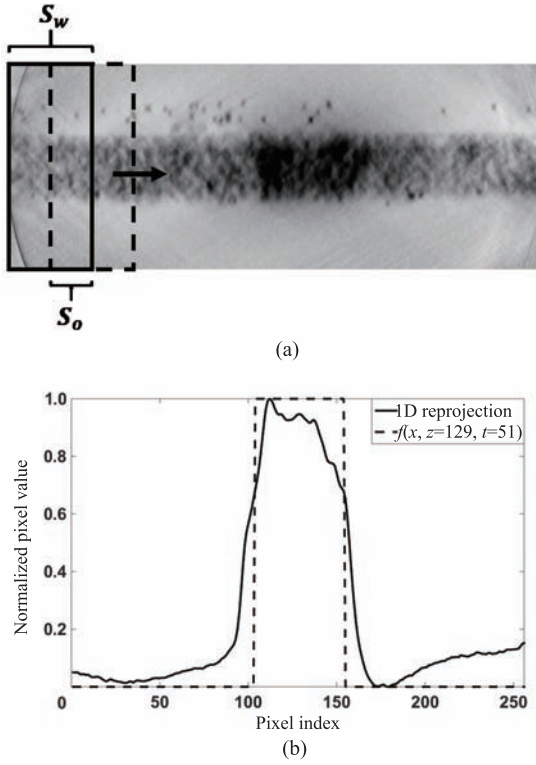
(a)

(b)

Fig. 4 Determination of z-shift and thickness corresponding to the test on resin-embedded ET dataset in Section 3.3. (a) Division of the X_{90}-re-projection with a sliding window; (b) normalized 1D re-projection and rectangular function.

by Eq. (2)). We determine the z-shift and thickness for each sub-image by solving an optimization problem, as shown in Eq. (3). Then, we use Eq. (4) and the maximum Normalized Correlation Coefficients (NCC) to generate weights for each sub-image, and calculate the overall z-shift d_z and thickness T using the weighted accumulation (Eqs. (5) and (6)). Practically speaking, it is better to reconstruct a volume with a thickness about 10 to 20 pixels greater than the actual thickness of the specimen[9]. In this paper, we determine a thickness that is 10 pixels greater than the specimen thickness.

$$f(x, z_i, t_i) = \begin{cases} 1, & z_i - \lfloor \frac{t_i}{2} \rfloor <= x <= z_i + \lceil \frac{t_i}{2} \rceil; \\ 0, & \text{otherwise} \end{cases} \quad (2)$$

$$\text{maxNCC}_i = \max_{z_i, t_i} \text{ncc}(\text{reproj1}D_i, f(z_i, t_i)),$$
$$\text{s.t.,} \quad z_i, t_i < s \quad (3)$$

where subscript i corresponds to the i-th sub-image, $\text{ncc}(\text{reproj1}D_i, f(z_i, t_i))$ calculates the NCC values between the 1D re-projection $\text{reproj1}D_i$ and $f(z_i, t_i)$, s

is the size of $\text{reproj1}D_i$, z_i and s are used to calculate the z-shift and t_i is thickness.

$$w_i = \frac{\text{maxNCC}_i}{\sum_j \text{maxNCC}_j} \quad (4)$$

$$d_z = \sum_i w_i \cdot \left(\frac{s}{2} - z_i \right) \quad (5)$$

$$T = \sum_i w_i \cdot t_i + 10 \quad (6)$$

In the "**Determine tilt angle offset**" step, the X_{90}-re-projection is used to calculate a series of z_i and w_i using Eqs. (3) and (4). The center positions c_i (on the X-axis) of each sub-image are also recorded. Then, we fit dataset (c_i, z_i) with a linear function using a weighted least squares method (Eq. (7)). The tilt-angle offset is determined using Eq. (8).

$$\min_{k,b} \sum_i w_i \cdot (z'_i - z_i)^2, z'_i = k \cdot c_i + b \quad (7)$$

$$\theta_{to} = \arctan(k),$$
$$k = \frac{\sum_i(w_i \cdot z_i) \sum_i(w_i \cdot c_i) - \sum_i(w_i \cdot z_i \cdot c_i)}{\sum_i(w_i \cdot c_i)^2 - \sum_i(w_i \cdot c_i^2)} \quad (8)$$

In the "**Determine azimuth angle**" step, we use the $-90°$ re-projection instead of the X_{90}-re-projection. The same procedure is used to determine the azimuth angle as that used to determine the tilt-angle offset.

3 Results and Discussion

3.1 Test dataset

We tested AutoGDeterm using simulated and resin-embedded ET datasets.

We generated simulated ET datasets using a Serial Block-face scanning Electron Microscopy (SBEM) 3D reconstruction of brain tissue extracted from a mouse cerebellum. The SBEM data was generated using a Zeiss Merlin scanning electron microscope equipped with an ultramicrotome (Gatan 3View system). Each image was collected by detecting the backscattered electrons, with the microscope operating at an acceleration voltage of 1.9 kV. During the acquisition process, we used a digital micrograph to automatically invert the contrast to make the images resemble transmission electron microscopy micrographs[26]. To test the precision of AutoGDeterm under different SNRs, we generated three simulated ET tilt series with different noise levels (noise-free, SNR=1 and SNR=0.5), as shown in Figs. 5a–5c. We generated
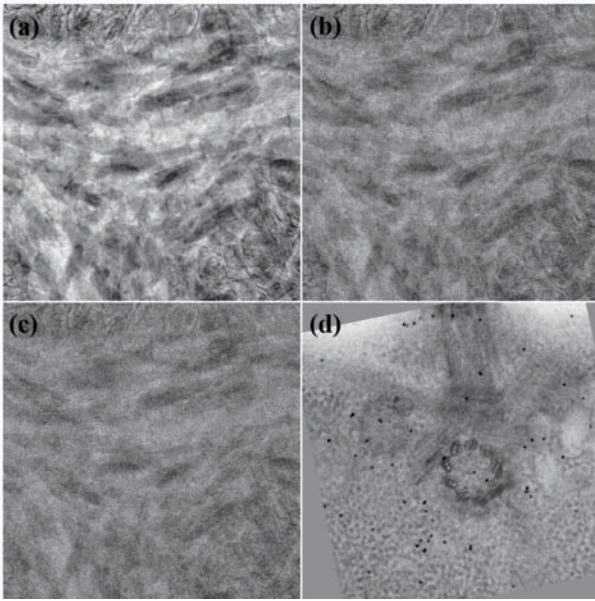
Fig. 5 **Test datasets. (a) Noise-free simulated dataset; (b) simulated dataset with SNR=1; (c) simulated dataset with SNR=0.5; (d) resin-embedded ET dataset.**

the tilt series using IMOD. The image size was 512×512 pixels and the tilt angles ranged from $-60°$ to $+60°$ with increments of $2°$. The simulated geometric parameters were 5 pixels for the z-shift, 63 pixels for the thickness, $2.2°$ for the azimuth angle, and $2.5°$ for tilt-angle offset.

We downloaded the resin-embedded ET dataset (file "BBa.st", Fig. 5d) from the IMOD website[9]. Fiducial markers were embedded in the dataset to guarantee accurate alignment. The original image size was 1000×1000 and the tilt angles ranged from $-60°$ to $+60°$ with $2°$ increments. In this paper, the image was binned with a factor of 2 and the final pixel size was 2.02 nm.

3.2 AutoGDeterm test using simulated dataset

In this section, we evaluate the precision of AutoGDeterm with three simulated aligned tilt series with known geometric parameters. We use the geometry determination module TOMOPITCH in IMOD[9] to illustrate the performance of AutoGDeterm, because IMOD is a successful and widely used ET suite. However, we note that, even with our best effort, the parameters determined using TOMOPITCH (by manually selecting the position features) may be subjective and the accuracy may be improved with more experienced operation. In practice, readers can choose geometry determination methods according to personal preference. The TOMOPITCH procedure can be briefly described as follows: first, several XZ-slices from the bottom, middle, and top areas of

the tomogram are reconstructed using WBP. Then, the position features are manually selected from these slices to generate a boundary model. Lastly, the geometric parameters are calculated using the boundary model. To reduce subjectivity, we repeated each TOMOPITCH determination ten times and used the average parameters for comparison.

First, we tested AutoGDeterm using the noise-free simulated dataset. Figures 6a–6c show the boundary model used in TOMOPITCH and Figs. 6d–6e show the re-projections used in AutoGDeterm. For the noise-free dataset, the reconstructed XZ-slices have a comparable contrast with the re-projections and the position features are sufficiently clear to be correctly identified. The accuracy of AutoGDeterm is comparable to that of TOMOPITCH (Table 1). For θ_{az} and θ_{to}, the errors of AutoGDeterm and TOMOPITCH are no greater than $0.2°$. The thicknesses of AutoGDeterm and TOMOPITCH are both about 10 pixels greater than the actual thickness. As for the z-shift, the error of AutoGDeterm is 1.4 pixels, which is slightly larger than that of TOMOPITCH (0.9 pixels). For visual validation, Figs. 6f and 6g show the corrected re-projections of AutoGDeterm.

Next, we tested AutoGDeterm with two noisy datasets (SNR=0.5, 1). To avoid duplication, Fig. 7 shows only the SNR=0.5 dataset determination. Because of the extremely high noise level, the reconstructed XZ-slices (Figs. 7a–7c) used in TOMOPITCH have poorer contrast than the ICON re-projections (Figs. 7d–7e), which still show clear position features. Low contrast makes it difficult to correctly identify position features from single reconstructed slice, which means greater effort is needed to make an accurate determination. As the noise level increases, the accuracies of TOMOPITCH and
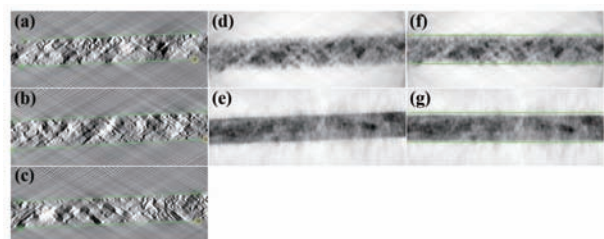

Fig. 6 **AutoGDeterm test using noise-free simulated dataset. (a–c) Boundary models used in TOMOPITCH; (d) X_{90}-re-projection used in AutoGDeterm; (e) $-90°$ re-projection used in AutoGDeterm; (f) corrected X_{90}-re-projection by AutoGDeterm; (g) corrected $-90°$ re-projection by AutoGDeterm.**

Table 1   Geometric parameters of simulated dataset determined using TOMOPITCH and AutoGDeterm.

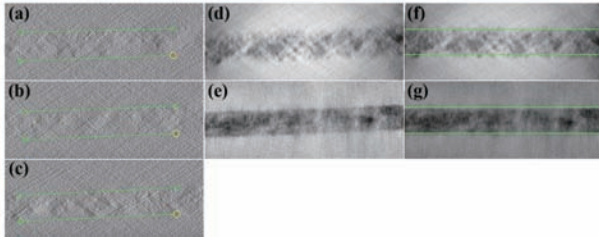| SNR	Simulated	θ_{az} (2.20)	θ_{to} (2.50)	Thickness (63)	z-shift (5)
Noise-free	TOMOPITCH	2.17 (−0.03)	2.39 (−0.11)	76 (+13)	5.9 (+0.9)
Noise-free	AutoGDeterm	2.26 (+0.06)	2.49 (−0.01)	73 (+10)	6.4 (+1.4)
1	TOMOPITCH	1.92 (−0.28)	2.72 (+0.22)	75 (+12)	6.1 (+1.1)
1	AutoGDeterm	2.35 (+0.15)	2.64 (+0.14)	71 (+8)	6.4 (+1.4)
0.5	TOMOPITCH	1.83 (−0.37)	2.28 (−0.22)	73 (+10)	6.5 (+1.5)
0.5	AutoGDeterm	2.29 (+0.09)	2.80 (+0.30)	70 (+7)	6.3 (+1.3)

Fig. 7   AutoGDeterm test using noisy simulated dataset (SNR=0.5). (a–c) Boundary models used in TOMOPITCH; (d) X_{90}-re-projection used in AutoGDeterm; (e) $-90°$ re-projection used in AutoGDeterm; (f) corrected X_{90}-re-projection by AutoGDeterm; (g) corrected $-90°$ re-projection by AutoGDeterm.
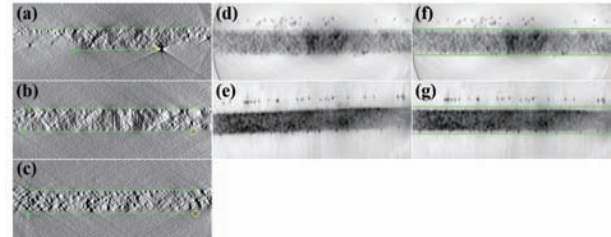

Fig. 8   AutoGDeterm test using resin-embedded ET dataset. (a–c) Boundary models used in TOMOPITCH; (d) X_{90}-re-projection used in AutoGDeterm; (e) $-90°$ re-projection used in AutoGDeterm; (f) corrected X_{90}-re-projection by AutoGDeterm; (g) corrected $-90°$ re-projection by AutoGDeterm.

AutoGDeterm decrease (Table 1). However, the accuracy of AutoGDeterm is comparable to that of TOMOPITCH and it generates a good correction (Figs. 7f and 7g).

3.3   AutoGDeterm test using resin-embedded ET dataset

Since the actual geometric parameters in real ET datasets are not known, we used the relative difference between AutoGDeterm and TOMOPITCH and visual validation to evaluate the accuracy of AutoGDeterm. Figures 8a–8e show the boundary models used in TOMOPITCH and the re-projections used in AutoGDeterm. Although the sample is slightly bent, the correction of the re-projections by AutoGDeterm is good (Figs. 8f and 8g), which demonstrates the robustness of AutoGDeterm with respect to sample deformation. Also, the absolute differences between TOMOPITCH and AutoGDeterm are small (Table 2), which demonstrates the comparable accuracy of AutoGDeterm to that of TOMOPITCH in the geometry determination of real ET dataset.

For visual validation, we reconstructed the tilt series using WBP and then corrected the reconstruction using the geometric parameters from TOMOPITCH and AutoGDeterm, respectively. Figure 9a shows the 281th XY-slice (the 256th XY-slice is the central slice) of

Table 2   Geometric parameters of resin-embedded ET dataset determined using TOMOPITCH and AutoGDeterm.

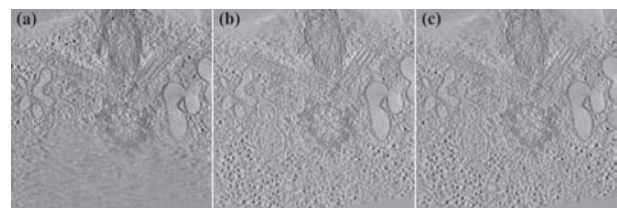|	θ_{az}	θ_{to}	Thickness	z-shift
TOMOPITCH	2.23	0.31	65	−0.4
AutoGDeterm	2.29	0.47	64	−1.49
abs (difference)	0.06	0.16	1	1.09

Fig. 9   Corrected reconstructions of TOMOPITCH and AutoGDeterm. (a) 281th XY-slice of uncorrected reconstruction; (b) 281th XY-slice of corrected reconstruction by TOMOPITCH; (c) 281th XY-slice of corrected reconstruction by AutoGDeterm.

an uncorrected tomogram, because of the azimuth angle, the bottom part of slice is out of the sample. Figures 9b and 9c show the same XY-slices of corrected tomograms, in which we can see that both corrections generate flat reconstructions and the AutoGDeterm result is visually identical to that of TOMOPITCH.

4 Conclusion

In this paper, we proposed an automatic ET geometry determination method, called AutoGDeterm. Our focus was to solve two key issues that arise in the use of the traditional "manual-positioning" method and to provide an automatic high-precision geometry determination framework by the introduction of ICON re-projections and a series of numerical analysis methods. We tested AutoGDeterm using simulated datasets and a resin-embedded dataset. The experimental results demonstrate that the accuracy of AutoGDeterm is high and comparable to that of TOMOPITCH.

However, we note that AutoGDeterm depends on a full reconstruction rather than the reconstruction of several slices, as performed by TOMOPITCH, which means more time is needed to complete AutoGDeterm's automatic geometry determination procedure. In future work, an improvement in speed will be made possible by employing several parts rather than a whole reconstruction in the determination.

References

[1] S. Asano, B. D. Engel, and W. Baumeister, *In situ* cryo-electron tomography: A post-reductionist approach to structural biology, *J. Mol. Biol.*, vol. 428, no. 2, pp. 332–343, 2016.

[2] J. A. G. Briggs, Structural biology *in situ* - the potential of subtomogram averaging, *Curr. Opin. Struct. Biol.*, vol. 23, no. 2, pp. 261–267, 2013.

[3] T. A. M. Bharat, C. J. Russo, J. Löwe, L. A. Passmore, and S. H. W. Scheres, Advances in single-particle electron cryomicroscopy structure determination applied to sub-tomogram averaging, *Structure*, vol. 23, no. 9, pp. 1743–1753, 2015.

[4] S. Pfeffer, L. Burbaum, P. Unverdorben, M. Pech, Y. X. Chen, R. Zimmermann, R. Beckmann, and F. Förster, Structure of the native sec61 protein-conducting channel, *Nat. Commun.*, vol. 6, p. 8403, 2015.

[5] R. M. Mersereau and A. V. Oppenheim, Digital reconstruction of multidimensional signals from their projections, *Proc. IEEE*, vol. 62, no. 10, pp. 1319–1338, 1972.

[6] H. Winkler and K. A. Taylor, Accurate marker-free alignment with simultaneous geometry determination and reconstruction of tilt series in electron tomography, *Ultramicroscopy*, vol. 106, no. 106, pp. 240–254, 2006.

[7] P. Penczek, M. Marko, K. Buttle, and J. Frank, Double-tilt electron tomography, *Ultramicroscopy*, vol. 60, no. 3, pp. 393–410, 1995.

[8] M. C. Lawrence, Least-squares method of alignment using markers, in *Electron Tomography*, J. Frank, ed. Springer, 1992, pp. 197–204.

[9] J. R. Kremer, D. N. Mastronarde, and J. R. Mcintosh, Computer visualization of three-dimensional image data using IMOD, *J. Struct. Biol.*, vol. 116, no. 1, pp. 71–76, 1996.

[10] J. Frank, *Electron Tomography*: *Methods for Three-Dimensional Visualization of Structures in the Cell*. Springer, 2006.

[11] F. Amat, F. Moussavi, L. R. Comolli, G. Elidan, K. H. Downing, and M. Horowitz, Markov random field based automatic image alignment for electron tomography, *J. Struct. Biol.*, vol. 161, no. 3, pp. 260–275, 2008.

[12] R. M. Han, L. S. Wang, Z. Y. Liu, F. Sun, and F. Zhang, A novel fully automatic scheme for fiducial marker-based alignment in electron tomography, *J. Struct. Biol.*, vol. 192, no. 3, pp. 403–417, 2015.

[13] R. Guckenberger, Determination of a common origin in the micrographs of tilt series in three-dimensional electron microscopy, *Ultramicroscopy*, vol. 9, nos. 1&2, pp. 167–173, 1982.

[14] Y. Liu, P. A. Penczek, B. F. McEwen, and J. Frank, A marker-free alignment method for electron tomography, *Ultramicroscopy*, vol. 58, nos. 3&4, pp. 393–402, 1995.

[15] H. Winkler and K. A. Taylor, Marker-free dual-axis tilt series alignment, *J. Struct. Biol.*, vol. 182, no. 2, pp. 117–124, 2013.

[16] S. Brandt, J. Heikkonen, and P. Engelhardt, Automatic alignment of transmission electron microscope tilt series without fiducial markers, *J. Struct. Biol.*, vol. 136, no. 3, pp. 201–213, 2001.

[17] R. M. Han, F. Zhang, X. H. Wan, J. J. Fernández, F. Sun, and Z. Y. Liu, A marker-free automatic alignment method based on scale-invariant features, *J. Struct. Biol.*, vol. 186, no. 1, pp. 167–180, 2014.

[18] S. Phan, J. Bouwer, J. Lanman, M. Terada, and A. Lawrence, Non-linear bundle adjustment for electron tomography, computer science and information engineering, in *Proc. 2009 WRI World Congress on Computer Science and Information Engineering*, Los Angeles, CA, USA, 2009, pp. 604–612.

[19] A. F. Lawrence, S. Phan, and M. Ellisman, Electron tomography and multiscale biology, in *Proc. 9th Int. Conf. Theory and Applications of Models of Computation*, Beijing, China, 2012, pp. 109–130.

[20] D. L. Donoho, Compressed sensing, *IEEE Trans. Inf. Theory*, vol. 52, no. 4, pp. 1289–1306, 2006.

[21] M. Lustig, D. Donoho, and J. M. Pauly, Sparse MRI: The application of compressed sensing for rapid MR imaging, *Magn. Reson. Med.*, vol. 58, no. 6, pp. 1182–1195, 1999.

[22] Y. C. Deng, Y. Chen, Y. Zhang, S. L. Wang, F. Zhang, and F. Sun, ICON: 3D reconstruction with 'missing-information' restoration in biological electron tomography, *J. Struct. Biol.*, vol. 195, no. 1, pp. 100–112, 2016.

[23] R. Gordon, R. Bender, and G. T. Herman, Algebraic reconstruction techniques (ART) for three-dimensional electron microscopy and x-ray photography, *J. Theor. Biol.*, vol. 29, no. 3, pp. 471–481, 1970.

[24] P. Gilbert, Iterative methods for the three-dimensional reconstruction of an object from projections, *J. Theor. Biol.*, vol. 36, no. 1, pp. 105–117, 1972.

[25] M. Radermacher, Weighted back-projection methods, in *Electron Tomography*, J. Frank, ed. Springer, 2006.

[26] X. H. Wan, T. Katchalski, C. Churas, S. Ghosh, S. Phan, A. Lawrence, Y. Hao, Z. Y. Zhou, R. J. Chen, Y. Chen, Z. Fa, and M. H. Ellisman, Electron tomography simulator with realistic 3d phantom for evaluation of acquisition, alignment and reconstruction methods, *J. Struct. Biol.*, vol. 198, no. 2, pp. 103–115, 2017.

Yu Chen is a PhD candidate at the Institute of Computing Technology and University of Chinese Academy of Sciences. He obtained the BS degree from Beijing Institute of Technology, China in 2013. His research interests include bioinformatics, biomedical image processing, and high-performance computing.

Zihao Wang is a PhD candidate at the Institute of Computing Technology and University of Chinese Academy of Sciences. He obtained the BS degree from Xiamen University, China in 2014. His research interests include bioinformatics, biomedical image processing, and high-performance computing.
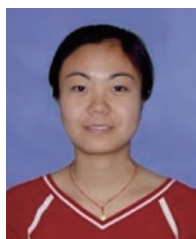
Xiaohua Wan is an associate professor at the Institute of Computing Technology, Chinese Academy of Sciences. She obtained the PhD degree in computer science form the Institute of Computing Technology, Chinese Academy of Sciences in 2012. Her research interests include bioinformatics, biomedical image processing, and high performance computing.

Fa Zhang is an associate professor at the Institute of Computing Technology, Chinese Academy of Sciences. He obtained the PhD degree in computer science form the Institute of Computing Technology, Chinese Academy of Sciences in 2005. His research interests include bioinformatics, biomedical image processing, and high performance computing.


Lun Li is a master student at the School of Mathematical Sciences, University of Chinese Academy of Sciences. He obtained the BS degree from Jilin University, China in 2013. His research interests include structural bioinformatics and deep learning.

Jingrong Zhang is a master student at the Institute of Computing Technology (ICT) and University of Chinese Academy of Sciences (UCAS). She obtained the BS degree from Yanshan University, China in 2012. Her research interests include high performance computing, deep learning, bioinformatics, and biomedical image processing.
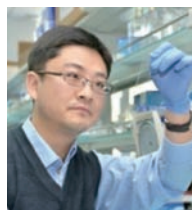
Fei Sun received the bachelor degree from Nanjing University, China in 2001 and obtained the PhD degree in biophysics from Tsinghua University in 2006. He established his lab at Institute of Biophysics (IBP), Chinese Academy of Sciences (CAS) in 2006. He is now a full professor of the National Key Laboratory of Biomacromolecules, IBP, CAS. He is also the chief scientist and director of the Center for Biological Imaging, IBP, CAS. His scientific research focuses on the structure of biomacromolecular complexes, membrane dynamics, and the development of three dimensional electron microscopy methodology. Currently, he is the vice president of the cryo-EM sub-society of Biophysical Society of China. He has authored more than 100 scientific papers.